

A New Formation Scenario for the Milky Way Cluster NGC 2419

R.C. Brüns and P. Kroupa

Argelander-Institut für Astronomie, Universität Bonn, Auf dem Hügel 71, D-53121 Bonn, Germany

rcbruens@astro.uni-bonn.de, pavel@astro.uni-bonn.de

ABSTRACT

We present a new formation scenario for NGC 2419, which is one of the most luminous, one of the most distant, and as well one of the most extended globular clusters of the Milky Way. We propose that NGC 2419 is the remnant of a merged star cluster complex, which was possibly formed during an interaction between a gas-rich galaxy and the Milky Way. To test this hypothesis, we performed numerical simulations of 27 different models of star cluster complexes (CCs) moving on a highly eccentric orbit in the Galactic halo. We vary the CC mass, the CC size, and the initial distribution of star clusters in the CC to analyze the influence of these parameters on the resulting objects.

In all cases, the vast majority of star clusters merged into a stable object. The derived parameters mass, absolute V-band magnitude, effective radius, velocity dispersion and the surface brightness profile are, for a number of models, in good agreement with those observed for NGC 2419. Despite the large range of CC sizes, the effective radii of the merger objects are constrained to a relatively small interval. A turnover in the r_{eff} vs. M_{encl} space leads to degenerate states, i.e. relatively compact CCs can produce an object with the same structural parameters as a more massive and larger CC. In consequence, a range of initial conditions can form a merger object comparable to NGC 2419 preventing us to pinpoint the exact parameters of the original CC, which formed NGC 2419.

We conclude that NGC 2419 can be well explained by the merged cluster complex scenario. Some of the recently discovered stellar streams in the Galactic halo might be related to the parent galaxy, which produced the cluster complex in our scenario. Measurements of the proper motion of NGC 2419 are necessary to prove an association with one of the stellar streams.

Subject headings: Galaxy: evolution — globular clusters: individual (NGC2419) — methods: numerical

1. INTRODUCTION

Globular clusters (GCs) are among the oldest radiant objects in the universe. They have typically compact sizes with half-light radii of a few pc and absolute V-band magnitudes between $M_V = -5$ to $M_V = -10$ corresponding roughly to masses between $10^4 M_\odot$ and $10^6 M_\odot$ (see Brodie & Strader 2006, and references therein).

The Milky Way has a rich GC system containing 150 GCs (Harris 1996). Only 13 GCs (or 9%) have an effective radius larger than 10 pc (see Figure 1). Most of these extended clusters (ECs) are fainter than about $M_V = -7$, only NGC 2419 has a high luminosity of about $M_V = -9.4$ mag. While all GCs with a comparable luminosity are quite compact, NGC 2419 has a projected half-light or effective radius of about 20 pc. The structural properties of NGC 2419 derived by various authors are displayed in Table 1. NGC 2419, located at $(l, b) = (180^\circ.4, 25^\circ.2)$, is one of the most metal-poor GCs with a metallicity of $[\text{Fe}/\text{H}] = -2.12$ (Harris 1996) at a Galactocentric distance of about 91.5 kpc and a heliocentric distance of 82.4 kpc (Harris 1996). NGC 2419 shows a single stellar population with an age of 12 to 13 Gyr (Salaris & Weiss 2002).

Figure 1 also shows the GCs from the LMC (Mackey & Gilmore 2004; van den Bergh & Mackey 2004), M51, and M81 (Chandar et al. 2004), from 68 dwarf galaxies of nearby loose galaxy groups (Georgiev et al. 2009), and the nearby elliptical galaxy NGC 5128 (Harris et al. 2002), as well as the ECs from M31 (Huxor et al. 2004; Mackey et al. 2006), M33 (Stonkutė et al. 2008), Scl-dE1 (Da Costa et al. 2009), and EC 90:12 from NGC 1399 (Richtler et al. 2005). It is evident that NGC 2419 has a rather isolated location in the M_V vs. r_{eff} space.

The unusual size and mass of NGC 2419 led to the speculation that NGC 2419 is not a GC, but the stripped core of a dSph galaxy captured by the Milky Way (e.g. van den Bergh & Mackey 2004). A stripped core should, however, show multiple stellar populations from the progenitor galaxy. In contrast, Ripepi et al. (2007) demonstrated that NGC 2419 shows no sign of multiple stellar populations and concluded that NGC 2419 is not a stripped core of a dwarf galaxy. Ripepi et al. (2007) also found that NGC 2419 is an Oosterhoff II cluster. They concluded that an extra-galactic origin of NGC 2419 is unlikely as the GCs of the Galactic dwarf galaxies usually show parameters between Oosterhoff types I and II. On the other hand, differences between NGC 2419 and typical values of GCs associated with Galactic dwarf spheroidal galaxies do not rule out an extra-galactic origin of NGC 2419 per se. For instance, five out of twelve GCs from the LMC are Oosterhoff II clusters (Catelan 2009).

High-resolution imaging of gas-rich galaxies experiencing major interactions using the Hubble Space Telescope has resolved regions with very intense star formation bursts. The bursting regions are typically located within the severely perturbed disks or tidal tails and are constrained to small complexes that contain a few to hundreds of young massive star clusters. Examples of such systems are the knots in the Antennae galaxies (Whitmore & Schweizer 1995; Whitmore et al. 1999), the complexes in the NGC 7673 star-burst (Homeier et al. 2002), M82 (Konstantopoulos et al. 2009), Arp 24 (Cao & Wu 2007), the “bird’s head galaxy” NGC 6745 (de Grijs et al. 2003), NGC 6946

(Larsen et al. 2002), Stephan’s Quintet (Gallagher et al. 2001), and NGC 922 (Pellerin et al. 2010).

The masses of such complexes vary from $10^6 M_\odot$ up to a few $10^8 M_\odot$. Bastian et al. (2006) observed star cluster complexes (CCs) in the Antennae with masses of the order $\approx 10^6 M_\odot$ and sizes of the order 100 to 200 pc. Pellerin et al. (2010) found young massive CCs with masses between $10^6 M_\odot$ and $10^{7.5} M_\odot$ and diameters between 600 pc and 1200 pc in the collisional ring galaxy NGC 922.

Mengel et al. (2008) observed individual young (≈ 10 Myr) star clusters associated with cluster complexes in the Antennae and NGC 1487. They compared dynamical mass estimates with derived photometric masses and found them in excellent agreement, implying that most of them survived the gas removal phase and are bound stellar objects. These young clusters are sufficiently stable to be used as building blocks for numerical simulations. Bastian et al. (2009) found three 200 to 500 Myr old, apparently stable clusters in the Antennae with very high radial velocities relative to the galactic disk, indicating that these star clusters will most likely become future halo objects. One cluster is surrounded by so far unmerged stellar features in its vicinity.

It has already been shown that CCs can merge to form a variety of spheroidal stellar-dynamical objects, such as ultra-compact dwarf galaxies (UCDs), faint fuzzies and possibly dwarf spheroidal galaxies (Kroupa 1998; Fellhauer & Kroupa 2002a,b; Brüns et al. 2009). In particular, the young UCD W3 is most naturally understood to be a merged massive CC (Fellhauer & Kroupa 2005).

In the present paper, we apply these ideas to NGC 2419 by analyzing how the structural parameters of the final merger objects in the outer Galactic halo correlate with the underlying CC parameters and compare them with the observed parameters of NGC 2419.

In Section 2, we describe the method and the parameters used for the calculations. Section 3 presents the results of the simulations, which will be discussed in Section 4. In Section 5 we provide a summary.

2. NUMERICAL METHOD AND SET-UP

The formation scenario described in this paper starts with newly born complexes of star clusters in the Galactic halo. We model the dynamical evolution of various CCs leading to merger objects. We do not, however, consider the galaxy-galaxy interaction, which formed the CCs in the first place.

2.1. The Code Superbox++

SUPERBOX++ developed by Metz (2008) is a new implementation of the particle-mesh code SUPERBOX (Bien et al. 1991; Fellhauer et al. 2000). Differences in the implementation of the algo-

rithm make the new code SUPERBOX++ much more efficient than the former. SUPERBOX had been implemented in the FORTRAN language with a particular focus on the minimization of usage of the random access memory (RAM), which is no longer a big issue in current days. SUPERBOX++ is now being implemented in the modern C++ programming language using object oriented programming techniques. The algorithm has been implemented with a focus on the performance of the code, but at the same time keeping memory consumption at a low level. SUPERBOX++ makes particular optimal use of modern multi-core processor technologies.

The code solves the Poisson equation on a system of Cartesian grids. The local universe is covered by a fixed coarse grid which contains the orbit of the CC around the center of the Milky Way. In order to get good resolution of the star clusters two grids with high and medium resolution are focused on each star cluster following their trajectories. The individual high resolution grids cover an entire star cluster, whereas the medium resolution grids of every star cluster embed the whole initial CC. All grids contain 128^3 grid cells. The CC orbits in an analytical Galactic potential (see Sect. 2.2.1). For each particle in the CC the acceleration from the galactic potential is added as an analytical formula to the grid-based acceleration computed by solving the Poisson equation. The coordinate system is chosen such that the disk of the Milky Way lies in the x-y-plane with origin at the Galactic center.

2.2. Orbit of NGC 2419

2.2.1. Gravitational Potential of the Milky Way

In our computations the Milky Way is represented by an analytical potential, which consists of a disk-, a bulge-, and a halo component.

The disk is modeled by a Miyamoto-Nagai potential (Miyamoto & Nagai 1975),

$$\Phi_{\text{disk}}(R, z) = -\frac{G M_d}{\sqrt{R^2 + (a_d + \sqrt{z^2 + b_d^2})^2}}, \quad (1)$$

with $M_d = 1.0 \times 10^{11} M_\odot$, $a_d = 6.5$ kpc, and $b_d = 0.26$ kpc. The bulge is represented by a Hernquist potential (Hernquist 1990),

$$\Phi_{\text{bulge}} = -\frac{G M_b}{r + a_b}, \quad (2)$$

with $M_b = 3.4 \times 10^{10} M_\odot$, and $a_b = 0.7$ kpc. The halo is a logarithmic potential,

$$\Phi_{\text{halo}}(r) = \frac{1}{2} v_0^2 \ln(r^2 + r_{\text{halo}}^2), \quad (3)$$

with $v_0 = 186.0 \text{ km s}^{-1}$, and $r_{\text{halo}} = 12.0$ kpc.

This set of parameters gives a realistic rotation curve for the Milky Way.

2.2.2. *Orbital Parameters*

The calculation of an orbit for NGC 2419 requires, next to the spatial coordinates, a good knowledge of the actual velocity vector of the cluster. As no proper motion measurements for NGC 2419 are available, the orbit cannot be properly fixed without major assumptions.

King (1962) suggested that the tidal radius of a GC is determined by the orbital position with the highest gravitational force, which is the perigalacticon. van den Bergh (1995) used this method to estimate a perigalactic distance of 20 kpc for NGC 2419. While this method provides only a very rough estimate of the perigalactic distance, we use it to narrow down the range of possible orbits.

NGC 2419 is one of the outermost Galactic GCs at a distance of $R_{\text{gal}} = 91.5$ kpc (Harris 1996). The very large distance and the observed low (heliocentric) negative radial velocity of $v_{\text{hel}} = -20.3$ km s⁻¹ (Baumgardt et al. 2009), which corresponds to a Galactic-standard-of-rest velocity of $v_{\text{GSR}} = -26.8$ km s⁻¹, suggests that NGC 2419 is close to its apogalacticon.

We choose a velocity vector for NGC 2419 in a way that it

- is consistent with the observed radial velocity,
- produces an orbit between Galactic radii 20 and about 92 kpc,
- is neither a polar orbit nor an orbit within the Galactic plane.

The velocity vector $(v_x, v_y, v_z) = (45 \text{ km s}^{-1}, -56 \text{ km s}^{-1}, 47 \text{ km s}^{-1})$ will be used as the current velocity vector of NGC 2419 for calculating the orbit.

Figure 2 shows the orbit of NGC 2419 calculated back in time using the Milky Way potential as given in Sect. 2.2.1. The orbital period is about 1.3 Gyr. The CC will most likely be formed during the first perigalactic passage of the parent galaxy. However, as the calculated objects will not change significantly after about 7 Gyr of evolution (see Sect. 3.1), we do not start at $t = -12$ Gyr (the age of NGC 2419) in order to cut down the computing time. For all numerical simulations we choose the perigalactic passage at $t = -9.568$ Gyr as a starting point.

2.3. **Initial Configuration of the Cluster Complex and Model Parameters**

The CC models consist of $N_0^{\text{CC}} = 20$ star clusters and are dived according to a Plummer distribution (Plummer 1911; Kroupa 2008). The cutoff radius, $R_{\text{cut}}^{\text{CC}}$, of the CC is four times the Plummer radius, $R_{\text{pl}}^{\text{CC}}$. The initial velocity distribution of the CC models is chosen such that the CC is in virial equilibrium. A detailed description of the generation of initial coordinates (space and velocity) for Plummer models is given in the appendix of Aarseth et al. (1974).

The individual star clusters building up the CCs in our simulations are Plummer spheres with a Plummer radius of $R_{\text{pl}}^{\text{SC}} = 4$ pc and a cutoff radius of $R_{\text{cut}}^{\text{SC}} = 20$ pc. Each star cluster has a mass

of $M^{\text{SC}} = 0.05 \times M^{\text{CC}}$ and consists of $N_0^{\text{SC}} = 100\,000$ particles. The velocity distribution of the individual star clusters is chosen to be initially in virial equilibrium.

In total, we considered 27 different models (see Tables 2 and 3), which are denoted M_{-x-y-z} , where x is the number of the initial configuration, i.e. the detailed distribution of the individual star clusters in the CC, y is the CC mass, M^{CC} , in units of $10^6 M_\odot$, and z is the CC Plummer radius, $R_{\text{pl}}^{\text{CC}}$, in pc. Figure 3 visualizes the CC parameter range covered in the M^{CC} vs. $R_{\text{pl}}^{\text{CC}}$ space. Figure 4 illustrates the different initial distributions. Figure 4a and b are the same initial distribution of star clusters that were scaled according to their $R_{\text{pl}}^{\text{CC}}$, while Figure 4c shows a less concentrated distribution of star clusters.

3. RESULTS

We carried out 27 different numerical simulations to get an estimate of the influence of varying initial CC conditions. All calculations start at the perigalactic passage at $t_0 = -9.568$ Gyr and are calculated up to the current position of NGC 2419.

3.1. Time Evolution of the Merging Process

The merging process of model $M_{-1-1.5-100}$ is shown in Figure 5 as contour plots on the xy-plane to illustrate the detailed evolution of the merging process. The snapshots were taken at $t' = t - t_0 = 0, 50, 100, 300, 760$ and 1500 Myr. At $t' = 50$ Myr the merger object is already in the process of forming, but the majority of star clusters are still individual objects. In the course of time more and more star clusters are captured by the merger object. Thus the merger object becomes more extended. After 10 crossing times ($t' = 760$ Myr) there are still 2 unmerged star clusters in the vicinity of the merger object. In the last snapshot at $t' = 1500$ Myr the merging process is completed and 19 out of 20 star cluster have merged forming a smooth extended object. One star cluster escaped the merging process. It follows the merger object on its orbit around the Milky Way at a distance of about 14 kpc (at $t' = 9.568$ Gyr).

The timescale of the merging process depends on the initial CC mass, the CC size and the distribution of star clusters within the CC. For model $M_{-1-1.5-100}$, 50 percent of the clusters have merged after approximately 100 Myr. The time within which half of the clusters merge increases with the CC size (from 15 Myr for model $M_{-1-1.5-25}$ to 200 Myr for model $M_{-1-1.5-150}$) and decreases with CC mass (from 150 Myr for model $M_{-1-1.0-100}$ to 65 Myr for model $M_{-1-3.0-100}$).

The further time evolution of the merger object of model $M_{-1-1.5-100}$ is plotted in Figure 6. The enclosed mass of the merger objects is defined as the mass within 800 pc. The half-mass radius is the radius of the sphere within which half of the mass is enclosed. However, as observers can only derive a projected half-mass radius, we calculate also a value projected on the sky defined

as the projected radius within which half of the mass is included. The projected half-mass radius is slightly smaller than the three-dimensional half-mass radius (Table 3) and corresponds to the observed effective radius, r_{eff} , if mass follows light. The effective radius and mass of the merger object decrease and become fairly constant after about 7 Gyr. The structural parameters change only very slightly in the next few Gyr.

3.2. Variation of initial CC mass and size

We consider models with three CC masses, $M^{\text{CC}} = 1.0, 1.5, \text{ and } 2.0 \times 10^6 M_{\odot}$, and six CC Plummer radii between $R_{\text{pl}}^{\text{CC}} = 25$ and 150 pc in steps of 25 pc to analyze the dependence of the structural parameters of the merger objects on the initial CC mass and size. In addition, two models with $R_{\text{pl}}^{\text{CC}} = 200$ and 300 pc are calculated for $M^{\text{CC}} = 2.0 \times 10^6$. All models have the same relative initial distribution of star clusters, which is scaled according to the respective Plummer radii (see Figure 4a and b). The velocities of the individual star clusters are also scaled with CC mass and size to keep the CCs initially in virial equilibrium.

For all models the merging process leads to a stable object. The number of merged star clusters is between 10 and 20. The properties of the merger objects at the current position of NGC 2419 are displayed in Table 3.

Figure 7a shows the enclosed mass, M_{encl} , of the merger objects as a function of the initial CC Plummer radius, $R_{\text{pl}}^{\text{CC}}$. The fraction of the initial CC mass, which is bound to the merger object, decreases almost linear with increasing CC size from about 92% at $R_{\text{pl}}^{\text{CC}} = 25$ pc for all three masses to values of 46, 53, and 59% at $R_{\text{pl}}^{\text{CC}} = 150$ pc for CC masses of $M^{\text{CC}} = 1.0, 1.5, \text{ and } 2.0 \times 10^6$, respectively. Mass-loss occurs either by the escape of individual stars from the diffuse stellar component, which builds up during the merging process (see Sect. 3.1), or by entire star clusters escaping the merging process. For all three masses, all 20 star clusters merge for compact models up to $R_{\text{pl}}^{\text{CC}} = 75$ pc, i.e. mass-loss is only from the diffuse component for these models. For the more extended models with $R_{\text{pl}}^{\text{CC}} \geq 100$ pc star clusters escape from the merging process. For extended models with $R_{\text{pl}}^{\text{CC}} = 150$ pc six, five, and two star clusters escape for CC masses of $M^{\text{CC}} = 1.0, 1.5, \text{ and } 2.0 \times 10^6$, respectively.

Figure 7b shows the effective radii, r_{eff} , of the merger objects as a function of the initial CC Plummer radius, $R_{\text{pl}}^{\text{CC}}$. The effective radii of the merger objects increase with increasing CC size up to $R_{\text{pl}}^{\text{CC}} = 75$ pc for $M^{\text{CC}} = 1.0 \times 10^6$ and up to $R_{\text{pl}}^{\text{CC}} = 100$ pc for the more massive models. For larger values of $R_{\text{pl}}^{\text{CC}}$ the effective radii decrease rapidly. Despite the large range of CC sizes ($R_{\text{pl}}^{\text{CC}} = 25$ to 300 pc), the effective radii of the merger objects are constrained to a relatively small interval, e.g. models with $M^{\text{CC}} = 2.0 \times 10^6$ are constrained to values between 13.2 and 25.6 pc.

Figure 8 combines Figures 7a and b showing the effective radius of the merger objects as a function of their enclosed mass. Only the six radii $R_{\text{pl}}^{\text{CC}} = 25, 50, 75, 100, 125, \text{ and } 150$ pc, where data for all three masses are available, were used to allow for an overview on the trends (models

with the same initial CC Plummer radius are connected by dotted lines, models with the same initial mass with solid lines). For all CC Plummer radii the effective radii increase with the initial CC mass. While the effective radii vary only slightly with mass for models with $R_{\text{pl}}^{\text{CC}} = 25, 50$ and 75 pc, the slope is considerably steepening for larger CC sizes.

The formation process of the merger objects depends on the compactness of the initial CC. A measure of how densely a CC is filled with star clusters for an equal number N_0^{CC} of star clusters is given by the parameter α (Fellhauer et al. 2002),

$$\alpha = \frac{R_{\text{pl}}^{\text{SC}}}{R_{\text{pl}}^{\text{CC}}}, \quad (4)$$

where $R_{\text{pl}}^{\text{SC}}$ and $R_{\text{pl}}^{\text{CC}}$ are the Plummer radius of a single star cluster and the Plummer radius of the CC, respectively. In our models, the individual star clusters are not scaled with $R_{\text{pl}}^{\text{CC}}$. This leads to decreasing values of α from 0.16 for $R_{\text{pl}}^{\text{CC}} = 25$ pc to $\alpha = 0.013$ for $R_{\text{pl}}^{\text{CC}} = 300$ pc. In general, large values of α accelerate the merging process because the star clusters already partly overlap in the center of the CC, whereas small values hamper the merging process.

Also the tidal field counteracts the merging process. An estimate of the influence of the tidal field on the CC is given by the parameter

$$\beta = \frac{R_{\text{cut}}^{\text{CC}}}{r_{\text{t}}^{\text{CC}}} \quad (5)$$

(Fellhauer et al. 2002), which is the ratio of the cutoff radius $R_{\text{cut}}^{\text{CC}}$ of the CC and its tidal radius r_{t}^{CC} . The tidal radius, r_{t}^{CC} , is defined as the radius where the attractive force of the CC on an object equals the pulling force of the Milky Way. Using the Milky Way potential as given in Section 2.2.1 and the CC potential, which is given by the Plummer potential

$$\Phi_{\text{pl}}^{\text{CC}}(r) = -G \frac{M^{\text{CC}}}{R_{\text{pl}}^{\text{CC}} \sqrt{(1 + \frac{r}{R_{\text{pl}}^{\text{CC}}})^2}}, \quad (6)$$

the tidal radius at the peri-galactic distance of 20 kpc is $r_{\text{t}}^{\text{CC}} = 296, 291, 283, 274$, and 262 pc for $M^{\text{CC}} = 1.5 \times 10^6$ and $R_{\text{pl}}^{\text{CC}} = 50, 75, 100, 125$ and 150 pc, respectively. The corresponding values of β are 0.68, 1.03, 1.41, 1.83 and 2.29. The values of β are slightly higher for the models with $M^{\text{CC}} = 1.0 \times 10^6$ and slightly lower for models with $M^{\text{CC}} = 2.0 \times 10^6$ (Table 4). The fraction of the enclosed mass of a merger object and the initial CC mass, $\frac{M_{\text{encl}}}{M^{\text{CC}}}$, is plotted as a function of β in Figure 9. The merger objects of the models for the three initial CC masses show the same linear correlation with β .

The models with $R_{\text{pl}}^{\text{CC}} = 75$ pc start already at the peri-galactic distance with a β of about one. Consequently, all 20 clusters merge. For the more extended models a number of star cluster are initially located outside the tidal radius. As we use a highly eccentric orbit, the CCs move rapidly towards larger Galactic distances, e.g. after 100 Myr they are at a distance of about 35 kpc. Due

to the lower gravitational field of the Milky Way at larger distances, the tidal radii increase leading to lower values of β . Figure 10 shows the variation of β with time for models with $M^{\text{CC}} = 1.5 \times 10^6$. For models M_1.1.5_100, M_1.1.5_125, and M_1.1.5_150 the period with $\beta > 1$ is getting longer, resulting in lower numbers of merged clusters for larger CCs. The turnover in r_{eff} , as shown in Figures 7b and 8, occurs at those $R_{\text{pl}}^{\text{CC}}$, where β is sufficiently large to allow entire star clusters to escape the merging process.

3.3. Variation of the initial distribution of star clusters

We use the CC parameters of model M_1.1.5_100 as a basis to analyze the influence of the detailed distribution of star clusters in the CC. We calculate the evolution of five additional models, of which two (M_2.1.5_100 and M_3.1.5_100) have a similar concentration of clusters in their center as M_1.1.5_100, whereas the other three models (M_4.1.5_100, M_5.1.5_100 and M_6.1.5_100) show a less concentrated distribution of star clusters (see Figure 4c). All six models result from exactly the same Plummer model but with different random number seeds.

The average and the standard deviation of the effective radii and enclosed masses of the merger objects of all six models are $r_{\text{eff}} = 23.8 \pm 3.2$ pc and $M_{\text{encl}} = 0.95 \pm 0.17 \times 10^6 M_{\odot}$, respectively. The standard deviations, which correspond to relative deviations of 13% (r_{eff}) and 18% (M_{encl}), provide an order of magnitude estimate of the influence of the distribution of star clusters on the structural parameters of the merger objects.

The merger objects resulting from compact initial configurations 1 to 3 have on average a significantly higher mass ($M_{\text{encl}} = 1.10 \pm 0.06 \times 10^6 M_{\odot}$) than the less concentrated configurations 4 to 6 ($M_{\text{encl}} = 0.81 \pm 0.06 \times 10^6 M_{\odot}$). In contrast, no clear difference in the effective radii of the merger objects can be seen between concentrated and extended initial distributions.

For comparison, an additional model M_7.1.5_200 has been calculated. It has a CC Plummer radius of 200 pc and a relatively small cutoff radius of 400 pc. A scaled version of model M_1.1.5_100 with $R_{\text{pl}}^{\text{CC}} = 200$ pc and a CC cutoff radius of 800 pc, which is four times the CC Plummer radius, would have 6 star clusters beyond 400 pc. Model M_7.1.5_200 has the same cutoff radius and therefore the same values of β as model M_1.1.5_100. Due to the broader initial distribution of star cluster in M_7.1.5_200 the enclosed mass and the effective radius are slightly lower than in model M_1.1.5_100.

The results demonstrate that next to the CC mass and the CC Plummer radius also the cutoff radius and the exact distribution of star clusters in a CC are key parameters for extended models, considerably influencing the structural parameters of the merger objects.

3.4. Comparison with Observations

The enclosed masses were converted into absolute V -magnitudes to allow for direct comparison with the observed data, using the formula

$$M_V = M_{V,\text{solar}} - 2.5 \times \log(M_{\text{encl}} \frac{L_V}{M}), \quad (7)$$

where, $M_{V,\text{solar}} = 4.83$ mag is the absolute solar V magnitude, M_{encl} the enclosed mass of the merger object and $\frac{M}{L_V}$ the mass-to-light ratio. We use a mass-to-light ratio of 2.05 ± 0.50 , as determined by Baumgardt et al. (2009) for NGC 2419. Apparent V -magnitudes can be calculated by adding the distance modulus of NGC 2419 $(m-M)_0 = 19.60$ (Ripepi et al. 2007) and a V -band extinction of $A_V = 0.25$ using a reddening of $E(B-V) = 0.08$ (Ripepi et al. 2007).

Figure 11 shows an exemplary contour plot of the merger object of model M_1.1.5_100 projected onto the sky using Galactic coordinates. The lowest contour line corresponds to $32 \text{ mag arcsec}^{-2}$. At this low surface brightness, NGC 2419 is detectable up to radii of about $17'$ corresponding to 415 pc . Observed photometry, however, covers only a region within the inner $60''$ of NGC 2419, while surface densities need to be derived from star counts in the outer parts. Ripepi et al. (2007) found evidence for stars associated with NGC 2419 up to radii of $15'$.

Figure 12 shows the effective radius, r_{eff} , versus the absolute magnitude, M_V , of the observations and the models as given in Table 1 and 3, respectively. Due to the scatter of the observed parameters of NGC 2419 and the turnover in the effective radii of the models as described in Section 3.2, a large number of models are compatible with the observed parameters of NGC 2419. Only extended models with initial CC masses of $M^{\text{CC}} = 1.0 \times 10^6$ and compact models with $M^{\text{CC}} = 2.0 \times 10^6$ are clearly incompatible with observations.

A more detailed comparison between models and observations can be achieved using surface brightness profiles. Bellazzini (2007) compiled a surface brightness profile out to projected radii of $477''.5$. However, as he used radii between $720''$ and $900''$, which are well inside NGC 2419, as a reference field to estimate the background level, Bellazzini's surface brightness estimates are expected to be slightly too faint in the outer parts NGC 2419.

The radial surface brightness profiles of four exemplary models projected onto the sky and converted to units of mag arcsec^{-2} are shown in Figure 13. The merger objects show a King-like profile out to radii of about $1000''$. The observed profile from Bellazzini (2007) is added to Figure 13 to allow for a direct comparison. The surface brightness profile of model M_1.1.0_50 agrees very well with the observed profile at all radii. The other three models in Figure 13 illustrate how the profiles change when one of the parameter mass, size and initial distribution of star clusters is modified. Model M_1.1.5_50 has a similar shape as M_1.1.0_50, but is too bright at all radii due to the larger mass. Model M_1.1.5_100, which is a more extended version of model M_1.1.5_50, agrees well with the observations between $10''$ and $100''$, but it is considerably brighter in the center and the outer parts. Model M_4.1.5_100, which has a broader initial distribution of star clusters than

model M_1.1.5_100, shows a smaller deviation from the observed surface brightness profile than model M_1.1.5_100.

Baumgardt et al. (2009) observed the radial velocities of 40 stars within a projected radius of 100 pc of NGC 2419 and derived a velocity dispersion of $\sigma = 4.14 \pm 0.48 \text{ km s}^{-1}$. The line-of-sight velocity dispersions within a projected radius of 100 pc of the models are listed in Table 3. A number of models with masses $M^{\text{CC}} = 1.0, 1.5, \text{ and } 2.0 \times 10^6 M_{\odot}$ have velocity dispersions that are within the one sigma error of the observed velocity dispersion. Model M_1.1.0_50, which has an effective radius and enclosed mass very close to the newest observed values from Baumgardt et al. (2009) and a surface brightness profile that is a good approximation of the observed profile, has a velocity dispersion of $\sigma = 4.13 \text{ km s}^{-1}$, i.e. almost exactly the observed one.

Considering masses, effective radii, surface brightness profiles, and velocity dispersions, model M_1.1.0_50 provides the best representation of NGC 2419. However, a number of models reproduce the observed structural parameters of NGC 2419 quite well within the observational uncertainties, demonstrating that an object like NGC 2419 can be formed from merged CCs without the need of fine-tuning of the input parameters.

4. DISCUSSION

4.1. The Merged Cluster Complex Scenario

The proposed formation scenario for NGC 2419 starts with newly born complexes of star clusters in the Galactic halo with orbital parameters allowing for an highly eccentric orbit. We model the dynamical evolution of various CCs leading to merger objects. We do not, however, consider the process which formed the CCs in the first place as this would increase the complexity of the simulations and add more degrees of freedom making the interpretation of the results difficult.

For all 27 models the majority of star clusters merge into a stable object. The turnover in the r_{eff} vs. M_{encl} space (Figure 7, 8 and 12) leads to degenerate states, because a relatively compact CC can produce a comparable merger object as a more massive CC having a significantly larger CC size. In consequence, a range of initial conditions can form a merger object comparable to NGC 2419 preventing us to pinpoint the parameters of the original CC, which formed NGC 2419. On the other hand, the larger the range of initial conditions that end up in a NGC 2419-like object, the larger is the probability of creating a massive EC like NGC 2419.

As the individual star clusters of the CC formed at approximately the same time from molecular clouds of a galaxy, the observed absence of multiple stellar populations (Ripepi et al. 2007) is fully consistent with our model. A small scatter in metallicity would also be explained, as the individual pre-cluster cloud cores of the complex could have had slightly different metallicities. In addition, some stars from the parent galaxy might have been captured by NGC 2419 during its formation as demonstrated for massive star clusters like ω Cen by Fellhauer et al. (2006).

Observations demonstrate that massive complexes of star clusters nowadays predominantly form during gravitational encounters between late-type galaxies. Young massive CCs with masses above $10^6 M_\odot$ and sizes of a few hundred pc, comparable to those used as initial conditions for the numerical simulations presented in Sect. 3, have been observed in the Antennae galaxies (Bastian et al. 2006) and in NGC 922 (Pellerin et al. 2010).

Since galaxy-galaxy mergers are anticipated to have been much more common during early hierarchical structure formation it is expected that star formation in cluster complexes has been a significant star formation mode during early cosmological epochs.

4.2. Potential Association with Stellar Streams in the Milky Way halo

As stellar structures in the outer halo are long lived features, remnants of a parent galaxy or stellar tidal streams may still be observable in the Milky Way halo.

Newberg et al. (2003) found an over-density of A-type stars at a distance of 83 to 85 kpc, which has a width of at least 10° and which was traced for more than 20° on the sky. NGC 2419 is located within this debris (on the sky and at the same distance). Newberg et al. (2003) argued that NGC 2419 and the stellar over-density might be associated with the Sagittarius dwarf galaxy, as NGC 2419 lies only 13 kpc from its orbital plane. However, the stellar streams from Sgr dwarf have mean metallicities between $[\text{Fe}/\text{H}] = -0.4$ near the core and -1.1 within the arms (Chou et al. 2007), while NGC 2419 has a very low metallicity of $[\text{Fe}/\text{H}] = -2.12$ (Harris 1996).

The Virgo Stellar Stream (VSS) has a metallicity of $[\text{Fe}/\text{H}] = -1.86$ with a large scatter of 0.40 dex (Duffau et al. 2006), which makes it comparable to the metallicity of NGC 2419. Casetti-Dinescu et al. (2009) determined the proper motion of the VSS and calculated an orbit with a pericentric distance of 11 kpc and an apocentric distance of 89 kpc. They concluded that the current position of NGC 2419 is compatible with this orbit.

Newberg et al. (2009) found a new stellar stream at a distance of 35 kpc in the constellation Cetus having a nearly polar orbit. The so-called Cetus Polar Stream (CPS) has a very low metallicity of $[\text{Fe}/\text{H}] = -2.1$. While the metallicity of CPS is in excellent agreement with NGC 2419, the polar orbit along Galactic longitude $l = 143^\circ$ appears to be in conflict with the current location of NGC 2419, which is at $l = 180^\circ$.

The Orphan Stream, independently discovered by Grillmair (2006) and Belokurov et al. (2006), has been analyzed in detail by Newberg et al. (2010). They found a very low metallicity of $[\text{Fe}/\text{H}] = -2.1$ and a likely orbit between a pericentric distance of 16.4 kpc and an apocentric distance of about 90 kpc. These parameters are very similar to those of NGC 2419.

Any potential association with the Sgr stream, VSS, CPS, or Orphan stream can only be verified after the proper motion of NGC 2419 has been measured.

4.3. NGC 2419-like Objects in other Galaxies

NGC 2419 is located in the outer Galactic halo. Also the lower mass ECs of the Milky Way are halo objects: 9 out of 13 ECs have galacto-centric distances greater than 20 kpc (Harris 1996). A similar trend has been shown for the other two disk galaxies in the Local Group: 12 out of 13 ECs associated with M31 and both ECs found in M33 have projected radii well outside the optical disks of these galaxies (Huxor et al. 2008; Stonkutė et al. 2008; Huxor et al. 2009). No EC as massive as NGC 2419 has been found in these galaxies.

Due to the limited field of view of the Hubble Space Telescope, most extragalactic studies on GCs cover only (a part of) the optical disk of the respective galaxies. An outer halo object like NGC 2419 would be found only by chance if it is projected onto the main body of a galaxy. Another reason for incompleteness is the difficulty of distinguishing ECs from background galaxies. Therefore, a number of surveys applied a size limit to reduce the contamination of background galaxies, e.g. the large GC surveys of the Virgo Cluster (Jordan et al. 2005) and the Fornax Cluster (Masters et al. 2010), covering dozens of galaxies. Their size limit of $r_{\text{eff}} < 10$ pc excludes all ECs from their GC catalogues.

While NGC 2419-like objects with masses of $M_{\text{EC}} \approx 10^6 M_{\odot}$ were not in the focus of extragalactic surveys, much effort has been made to detect and to analyze stellar objects of $M \approx 10^7 M_{\odot}$ since the discovery of ultra-compact dwarf galaxies (UCDs) in the Fornax Cluster by Hilker et al. (1999) and Drinkwater et al. (2000). A number of massive stellar objects with effective radii of $r_{\text{eff}} \approx 20$ pc have been found in the Fornax and the Virgo cluster (Mieske et al. 2008; Hasegan et al. 2005; Evstigneeva et al. 2007).

Richtler et al. (2005) present a NGC 2419-like object in the halo of the elliptical galaxy NGC 1399 which is the central galaxy of the Fornax Cluster. This object, labeled 90:12 in Richtler et al. (2005), is located at a projected distance of about 40 kpc and has a very blue color indicating a very low metallicity. It has an absolute V-band magnitude of $M_V = -10.04$ mag, which corresponds to a mass of $M_{90:12} = 1.8 \times 10^6 M_{\odot}$, assuming the same mass-to-light ratio as NGC 2419. The effective radius of $r_{\text{eff}} = 27$ pc is larger than that of NGC 2419. In Figure 12, this EC is located between the values of models M_1_2.0_100 and M_1_3.0_100. Therefore, the parameters of EC 90:12 are consistent with being a more massive version of NGC 2419.

Considerably larger and more complete datasets of stellar halo objects like ECs and UCDs are necessary to draw statistically significant conclusions on the question whether NGC 2419 is a low-mass UCD, or a high-mass EC, and whether they are all remnants of merged CCs. A parametric study covering the entire mass range from ECs to UCDs ($M^{\text{CC}} = 10^{5.5}$ to $10^8 M_{\odot}$) will be presented in a subsequent paper (Brüns et al. 2011).

5. SUMMARY

The Galactic globular cluster NGC 2419 has unique parameters. It is one of the most luminous, one of the most distant, and as well one of the most extended GCs of the Milky Way. Apart from these unusual parameters, NGC 2419 appears to be a normal Galactic GC having a low metallicity and a single stellar population.

We propose a new formation scenario for NGC 2419, being a remnant of a merged star cluster complex, which was formed during an interaction between a gas-rich galaxy and the Milky Way. To test this hypothesis, we performed particle-mesh-code computations of 27 different CC models. We vary the CC mass, the CC size, and the initial distribution of star clusters in the CC to analyze the influence of these parameters on the resulting objects. These CCs are comparable to those observed in the Antennae galaxies (Bastian et al. 2006) and in NGC 922 (Pellerin et al. 2010).

For all 27 models, the vast majority of star clusters merged into a stable object. The derived parameters mass, absolute V-band magnitude, effective radius, velocity dispersion and the surface brightness profile are, for a number of models, in good agreement with those observed for NGC 2419.

The effective radii of the merger objects increase with increasing CC size up to $R_{\text{pl}}^{\text{CC}} = 75$ pc for $M^{\text{CC}} = 1.0 \times 10^6$ and up to 100 pc for the more massive models. For larger values of $R_{\text{pl}}^{\text{CC}}$ the effective radii decrease rapidly (Figure 7). The turnover in the r_{eff} vs. M_{encl} space (Figures 8 and 12) leads to degenerate states, as relatively compact CCs can produce a comparable merger object as a more massive CC having a significantly larger size. Despite the large range of CC sizes ($R_{\text{pl}}^{\text{CC}} = 25$ to 300 pc) of the models with initial CC masses of $M^{\text{CC}} = 2.0 \times 10^6$, the effective radii of the merger objects are constrained to values between 13.2 and 25.6 pc.

In consequence, a range of initial conditions can form a merger object comparable to NGC 2419 preventing us to pinpoint the parameters of the original CC, which formed NGC 2419. On the other hand, the larger the range of initial conditions that end up in a NGC 2419-like object, the larger is the probability of creating a massive EC like NGC 2419.

Due to the limited field of view of the Hubble Space Telescope, most extragalactic studies on GCs cover only (a part of) the optical disk of the respective galaxies. An outer halo object like NGC 2419 would be found only by chance if it is projected onto the main body of a galaxy. Another reason for incompleteness is the difficulty of distinguishing ECs from background galaxies. Therefore, a number of surveys applied a size limit of about 10 pc to reduce the contamination of background galaxies. Thereby these surveys exclude all NGC 2419-like ECs from their GC catalogues. As massive galaxy-galaxy interactions are expected to have been more numerous in the past, a large number of NGC 2419-like objects probably await their detection in the outer halos of various galaxies.

We conclude that NGC 2419 can be well explained by the merged cluster complex scenario. Measurements of the proper motion of NGC 2419 are indispensable to further study the proposed scenario and to potentially associate NGC 2419 with one of the stellar streams in the outer Galactic

halo.

We thank Manuel Metz for providing his SUPERBOX++ code and his for excellent support. We thank the anonymous referee for his helpful comments that helped us to improve the paper significantly. The work of this paper was supported by DFG Grants KR 1635/14-1 and KR 1635/29-1.

REFERENCES

- Aarseth, S.J., Henon, M., & Wielen, R. 1974, *A&A*, 37, 183
- Bastian, N., Emsellem, E., Kissler-Patig, M., & Maraston, C. 2006, *A&A*, 445, 471
- Bastian, N., Trancho, G., Konstantopoulos, I.S. Miller, B.W. 2009, *ApJ*, 701, 607
- Baumgardt, H., Côté, P., Hilker, M., Rejkuba, M., Mieske, S., Djorgovski, S.G., & Stetson, P. 2009, *MNRAS*, 396, 2051
- Bellazzini, M. 2007, *A&A*, 473, 171
- Belokurov, V. et al. 2006, *ApJ*, 642, L137
- Bien, R., Fuchs, B., Wielen, R. 1991, in *CP90 Europhysics Conference on Computational Physics*, ed. Tenner (Singapore, World Scientific), 3
- Brodie, J. P., & Strader, J. 2006, *ARA&A*, 44, 193
- Brüns, R. C., Kroupa, P., & Fellhauer, M. 2009, *ApJ*, 702, 1268
- Brüns, R. C., Kroupa, P., Fellhauer, M., Metz, M., & Assmann, P. 2011, *A&A*, submitted
- Cao, C., & Wu, H. 2007, *AJ*, 133, 1710
- Casetti-Dinescu, D.I., Girard, T.M., Majewski, S.R., Vivas, A.K., Wilhelm, R., Carlin, J.L., Beers, T.C., & vanAltena, W.F. 2009, *ApJ*, 701, L29
- Catelan, M. 2009, *Ap&SS*, 320, 261
- Chandar, R., Whitmore, B., & Lee, M. G. 2004, *ApJ*, 611, 220
- Chou, M.-Y. et al. 2007, *ApJ*, 670, 346
- Da Costa, G. S., Grebel, E. K., Jerjen, H., Rejkuba, M., & Sharina, M.E. 2009, *AJ*, 137, 4361
- de Grijs, R., Anders, P., Bastian, N., Lynds, R., Lamers, H.J.G.L.M., & O’Neil, E.J. 2003, *MNRAS*, 343, 1285

- Drinkwater, M. J., Jones, J. B., Gregg, M. D., Phillipps, S. 2000, PASA, 17, 227
- Duffau, S., Zinn, R. Vivas, A. K., Carraro, G., Méndez, R.A., Winnick, R., & Gallart, C. 2006, ApJ, 636, L97
- Evstigneeva, E. A., Gregg, M. D., Drinkwater, M. J., Hilker, M. 2007, AJ, 133, 1722
- Fellhauer, M., Kroupa, P., Baumgardt, H., Bien, R., Boily, C. M., Spurzem, R., & Wassmer, N. 2000, New A, 5, 305
- Fellhauer, M., Baumgardt, H., Kroupa, P., & Spurzem, R. 2002, CeMDA, 82, 113
- Fellhauer, M., & Kroupa, P. 2002a, MNRAS, 330, 642
- Fellhauer, M., & Kroupa, P. 2002b, AJ, 124, 2006
- Fellhauer, M., & Kroupa, P. 2005, MNRAS, 359, 223
- Fellhauer, M., Kroupa, P., & Evans, N. W. 2006, MNRAS, 372, 338
- Gallagher, S. C., Charlton, J. C., Hunsberger, S. D., Zaritsky, D., & Whitmore, B.C. 2001, AJ, 122, 163
- Georgiev, I.Y., Puzia, T.H., Hilker, M., Goudfrooij, P. 2009, MNRAS, 392, 879
- Grillmair, C. J. 2006, ApJ, 645, L37
- Harris, W.E. 1996, AJ, 112, 1487
- Harris, W.E., Harris, G.L.H., Holland, S.T., & McLaughlin, D.E. 2002, AJ, 124, 1435
- Harris, W.E. 2009, ApJ, 699, 254
- Hasegan, M. et al. 2005, ApJ, 627, 203
- Hernquist, L. 1990, ApJ, 356, 359
- Hilker, M., Infante, L., Vieira, G., Kissler-Patig, M., & Richtler, T. 1999, A&AS, 134, 75
- Homeier, N., Gallagher, J. S. III, & Pasquali, A. 2002, A&A, 391, 857
- Huxor, A., Tanvir, N. R., Irwin, M., Ferguson, A., Ibata, R., Lewis, G., & Bridges, T. 2004, ASPC, 327, 118
- Huxor, A. P., Tanvir, N. R., Ferguson, A. M. N., Irwin, M.J., Ibata, R., Bridges, T., & Lewis, G.F. 2008, MNRAS, 385, 1989
- Huxor, A., Ferguson, A.M.N., Barker, M.K., Tanvir, N.R., Irwin, M.J., Chapman, S.C., Ibata, R., Lewis, G. 2009, ApJ, 698, 77

- Jordan, A., Ct, P., Blakeslee, J.P., Ferrarese, L., McLaughlin, D.E., Mei, S., Peng, E.W., Tonry, J.L., Merritt, D., Milosavljevic, M., Sarazin, C.L., Sivakoff, G.R., West, M.J. 2005, ApJ, 634, 1002
- King, I. 1962, AJ, 67, 471
- Konstantopoulos, I. S., Bastian, N., Smith, L. J., Tranco,G., Westmoquette,M.S., & Gallagher,J.S. 2009, ApJ, 701, 1015
- Kroupa, P. 1998, MNRAS, 300, 200
- Kroupa, P. 2008, in The Cambridge N-Body Lectures, Lecture Notes in Physics, Vol. 760, eds. S. Aarseth, C. Tout, & R. Mardling (Berlin: Springer Verlag), 181
- Larsen, S. S., Efremov, Y. N., Elmegreen, B. G., Alfaro,E.J., Battinelli,P., Hodge,P.W., & Richtler,T. 2002, ApJ, 567, 896
- Mackey, A. D., & Gilmore, G. F 2004, MNRAS, 352, 153
- Mackey, A. D. et al. 2006, ApJ, 653, L105
- Masters, K.L., Jordan, A., Ct, P., Ferrarese, L., Blakeslee, J.P., Infante, L., Peng, E.W., Mei, S., West, M. 2010, ApJ, 715, 1419
- McLaughlin, D. E., & van der Marel, R. P. 2005, ApJS, 161, 304
- Mengel, S., Lehnert, M. D., Thatte, N. A., Vacca,W.D., Whitmore,B., & Chandar,R. 2008, A&A, 489, 1091
- Metz, M. 2008, PhD thesis, Universität Bonn
- Mieske, S. et al. 2008, A&A, 487, 921
- Miyamoto, M., & Nagai, R. 1975, PASJ, 27, 533
- Newberg, H.J. et al. 2003, ApJ, 596, L191
- Newberg, H.J., Yanny, B., & Willett, B.A. 2009, ApJ, 700, L61
- Newberg, H.J., Willett, B.A., Yanny, B., & Xu, Y. 2010, ApJ, 711, 32
- Pellerin, A., Meurer, G. R., Bekki, K., Elmegreen, D. M., Wong, O. I., & Knezek, P. M. 2010, AJ, 139, 1369
- Plummer, H. C. 1911, MNRAS, 71, 460
- Richtler, T., Dirsch, B., Larsen, S., Hilker, M., Infante, L. 2005, A&A, 439, 533
- Ripepi, V. et al. 2007 ApJ, 667, L61

Salaris, M., & Weiss, A. 2002, *A&A*, 388, 492

Stonkutė, R. et al. 2008, *AJ*, 135, 1482

van den Bergh, S. 1995, *AJ*, 110, 1171

van den Bergh, S., & Mackey, A. D. 2004, *MNRAS*, 354, 713

Whitmore, B. C., & Schweizer, F. 1995, *AJ*, 109, 960

Whitmore, B. C., Zhang, Q., Leitherer, C., Fall, S. M., Schweizer, F., & Miller, B. W. 1999, *AJ*, 118, 1551

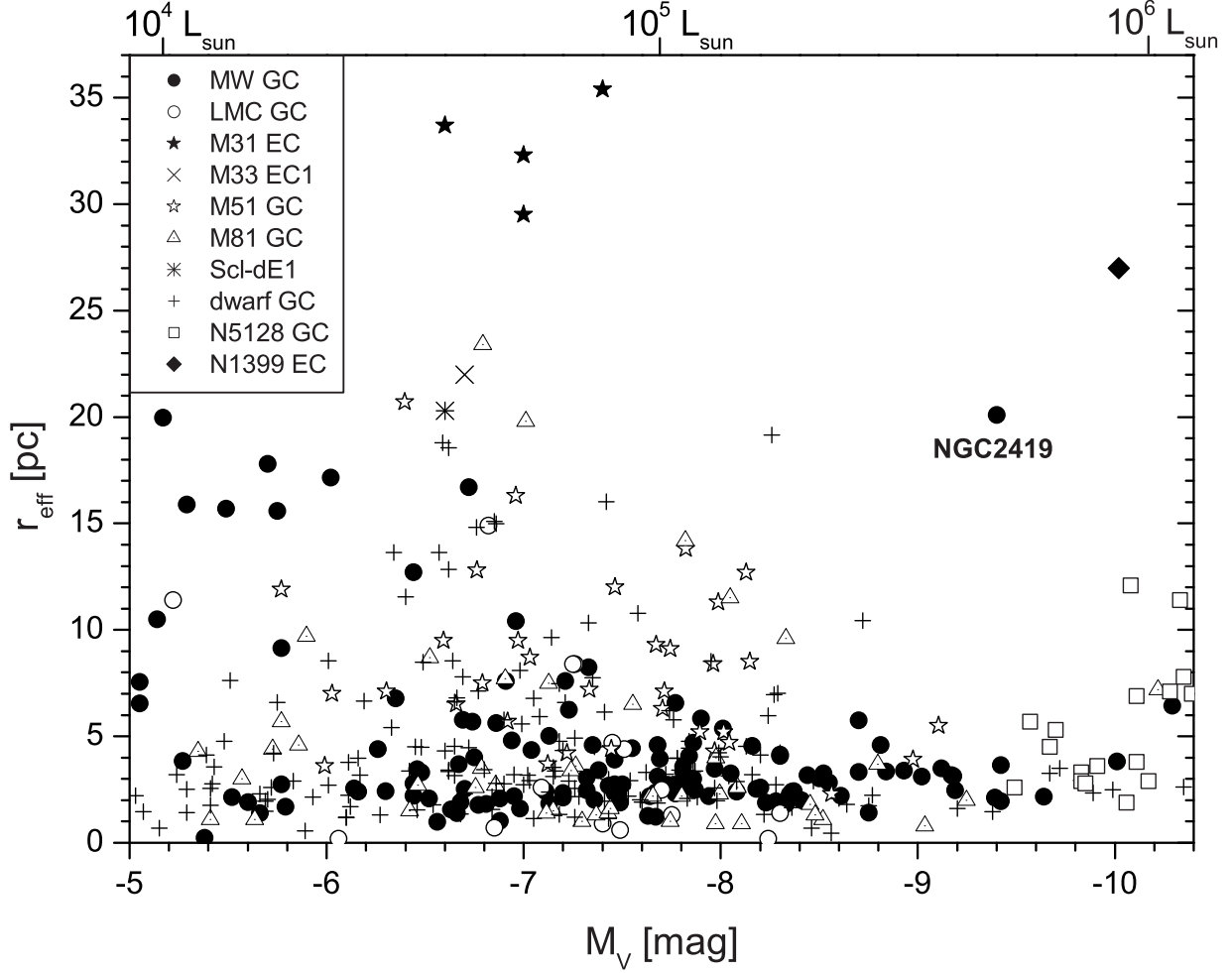


Fig. 1.— Overview of GCs of the Milky Way (Harris 1996), the LMC (Mackey & Gilmore 2004; van den Bergh & Mackey 2004), M51, and M81 (Chandar et al. 2004), NGC 5128 (Harris et al. 2002), 68 dwarf galaxies (Georgiev et al. 2009) and the ECs from M31 (Huxor et al. 2004; Mackey et al. 2006), M33 (Stonkutė et al. 2008), Scl-dE1 (Da Costa et al. 2009), and one EC from NGC 1399 (Richtler et al. 2005) in the r_{eff} vs. M_V space. NGC 2419 is in a rather isolated position.

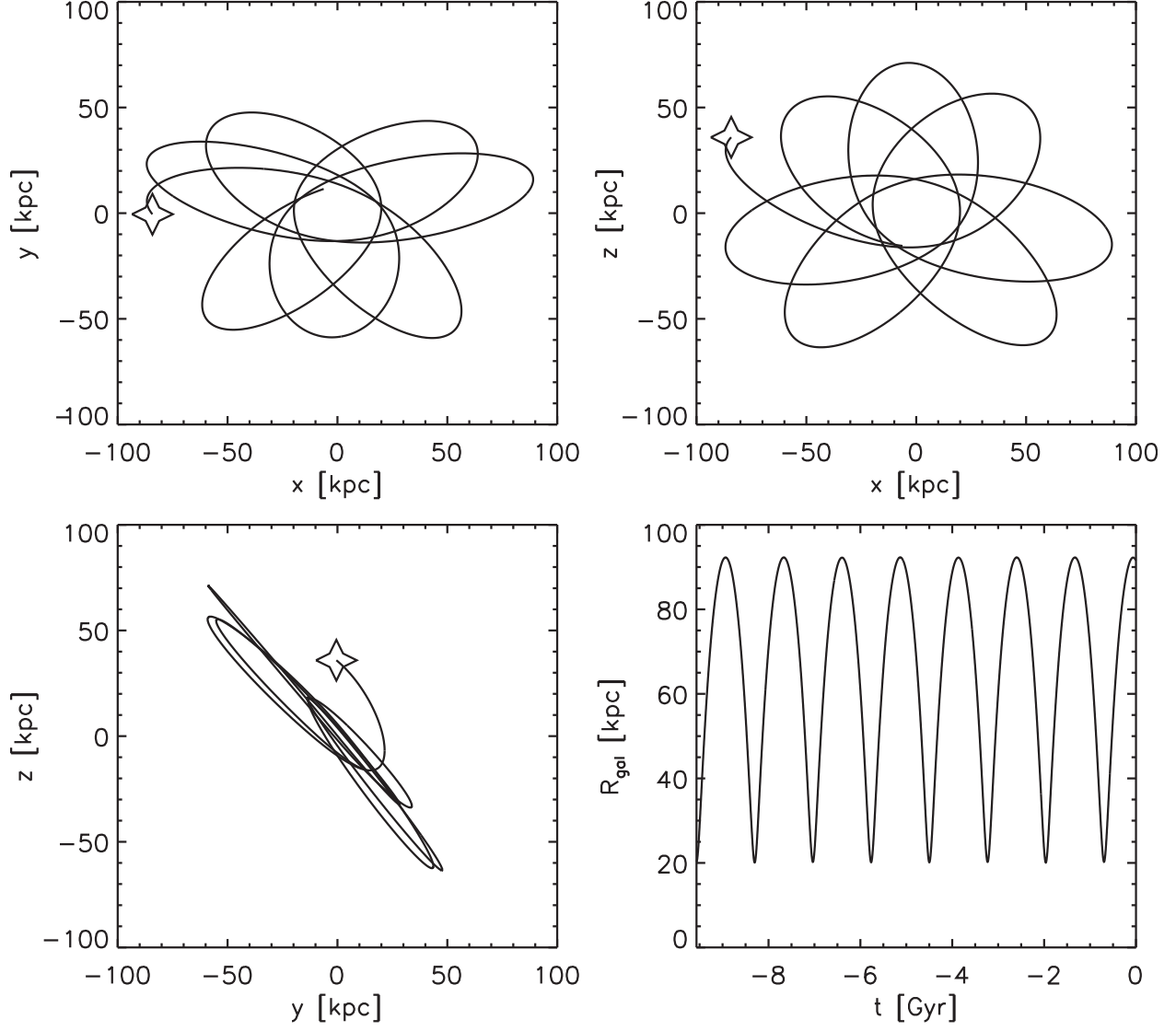


Fig. 2.— The orbit of NGC 2419 traced back from its current position and projected to the xy-, the xz-, and the yz-plane. The stars indicate the observed current position of NGC 2419. Lower left: The distance of NGC 2419 to the Galactic center. The orbital period is about 1.3 Gyr.

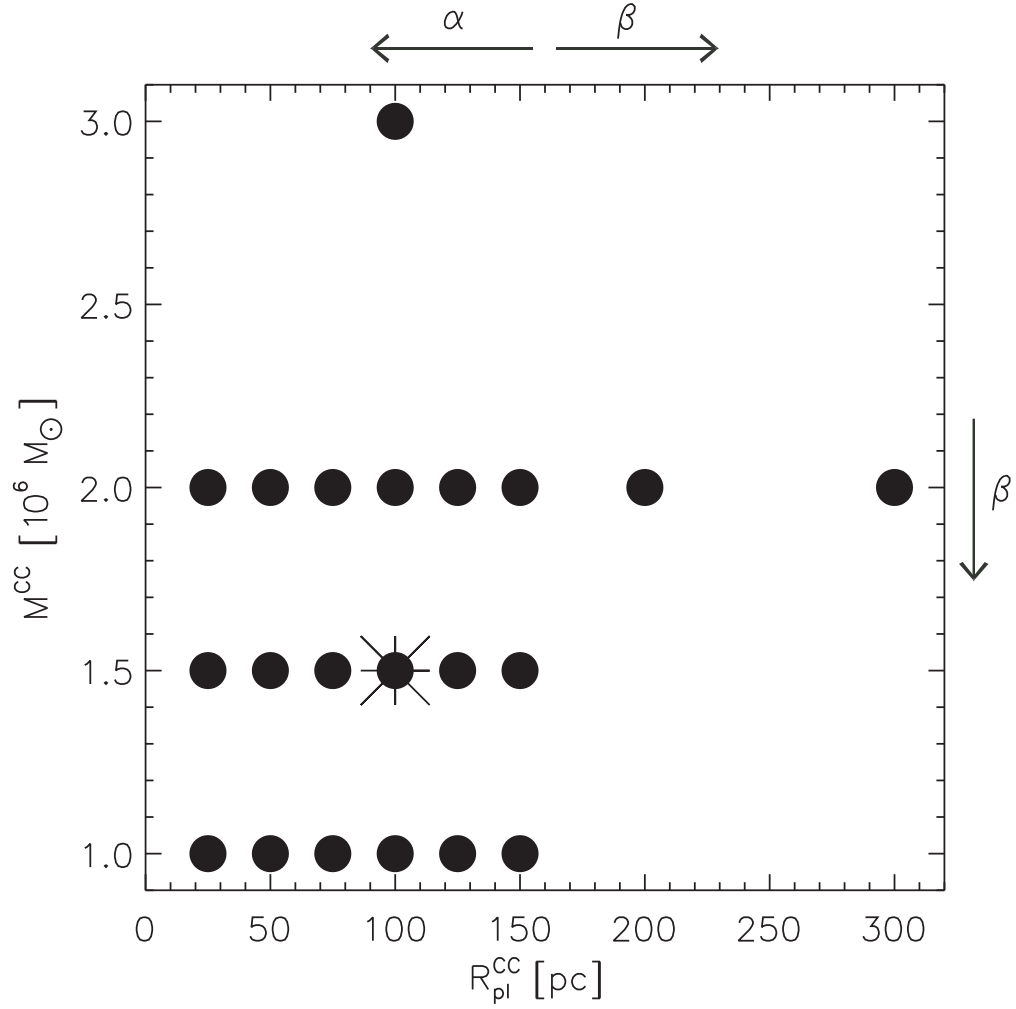


Fig. 3.— The parameter range covered in the M^{CC} vs. $R_{\text{pl}}^{\text{CC}}$ space. The arrows indicate the increase of the parameters α and β (see Sect. 3.2). The circle with the additional asterisk marks the values of M^{CC} and $R_{\text{pl}}^{\text{CC}}$ of those models, where the initial distribution of star clusters within the CC was varied (see Sect. 3.3).

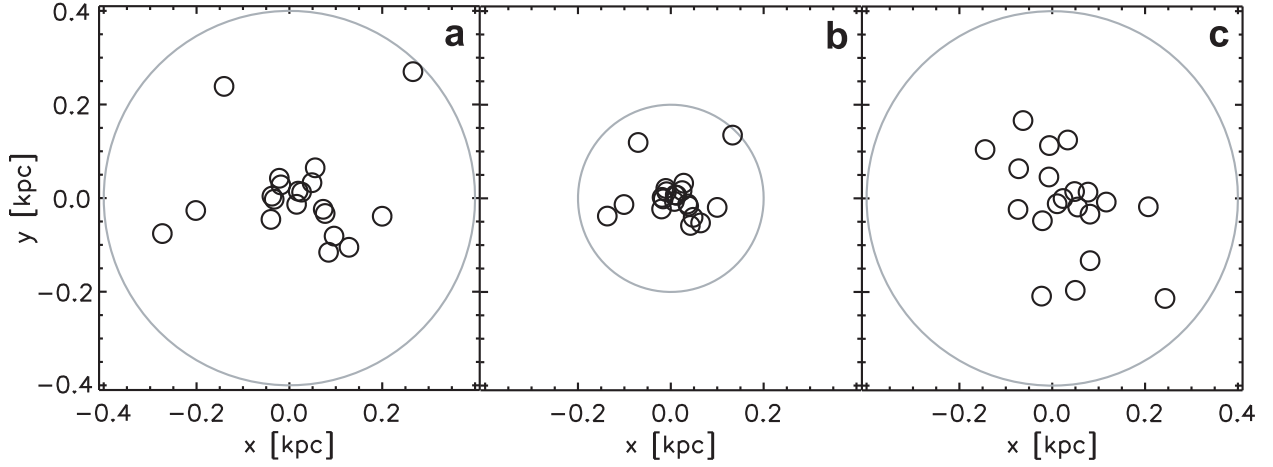


Fig. 4.— Three exemplary initial distributions of star clusters (small circles with radius $R_{\text{cut}}^{\text{SC}}$) in a CC (surrounding circle with radius $R_{\text{cut}}^{\text{CC}}$) projected onto the x-y-plane. Model M_1.1.5_50 (b) is a scaled version of M_1.1.5_100 (a) only differing in Plummer radius $R_{\text{pl}}^{\text{CC}}$. Some star clusters do already overlap in the center at the beginning. Model M_4.1.5_100 (c) has a less concentrated distribution of clusters than M_1.1.5_100.

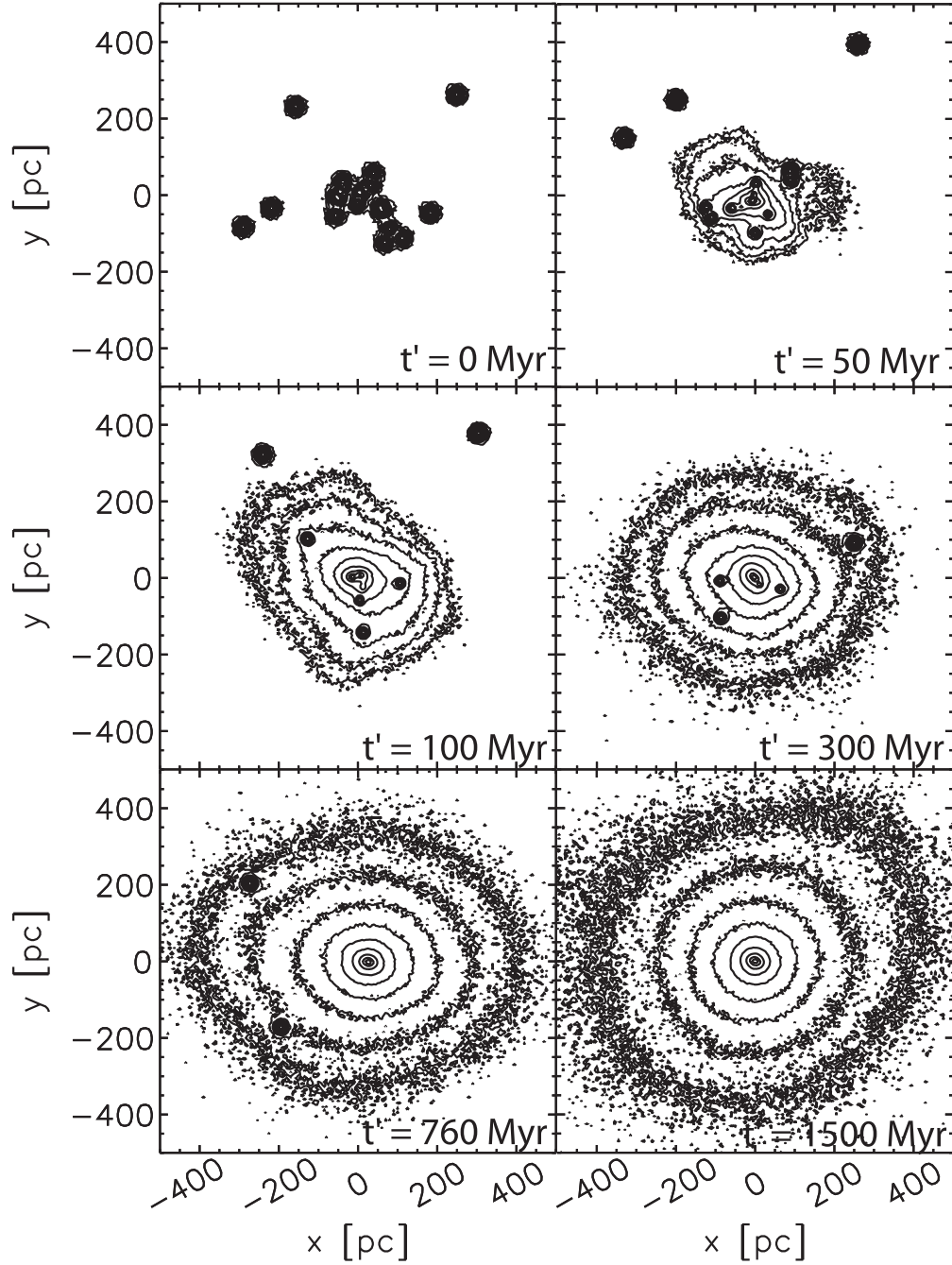


Fig. 5.— Time evolution of the merger object in model M_1.1.5_100. Contour plots on the x-y-plane displayed at $t' = 0, 50, 100, 300, 760$ and 1500 Myr. The lowest contour level corresponds to 5 particles per pixel. The pixel size is 5 pc. This yields $0.15 M_{\odot} \text{ pc}^{-2}$. The contour levels increase further by a factor of 3.

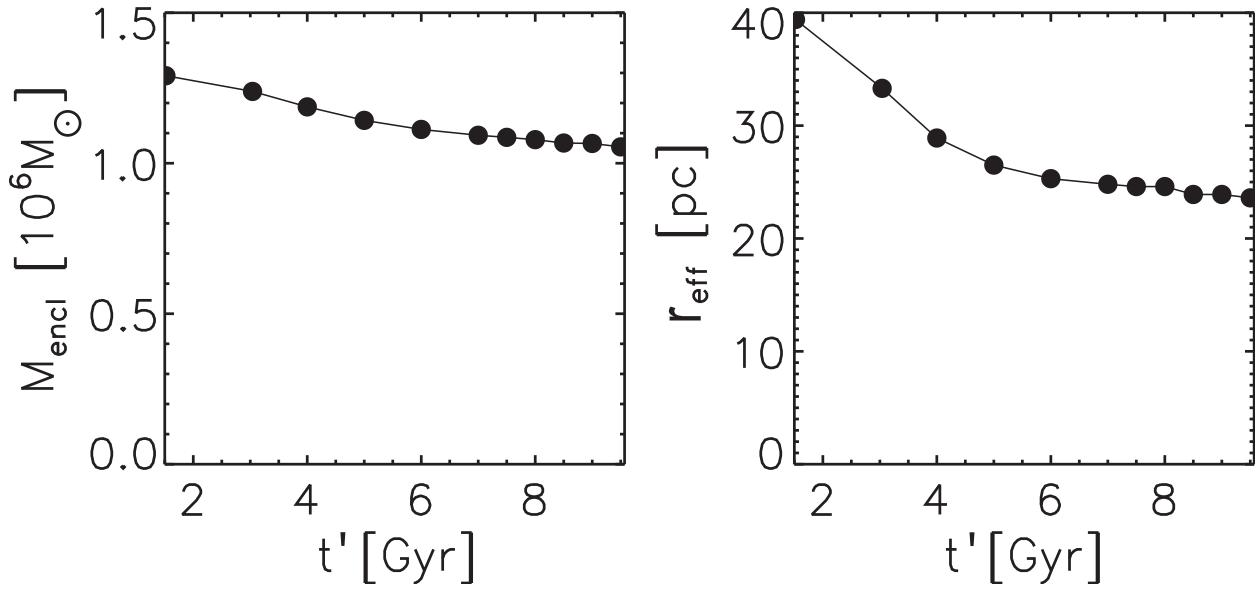


Fig. 6.— Left: Enclosed mass versus time after 1.5 Gyr of evolution of model M_1.1.5_100. The curve becomes fairly flat with increasing time. An almost stable merger object forms suffering only slightly from mass loss. Right: effective radius against time after 1.5 Gyr of evolution of model M_1.1.5_100. The effective radius decreases with time up to about 7 Gyr. Thereafter it is almost constant.

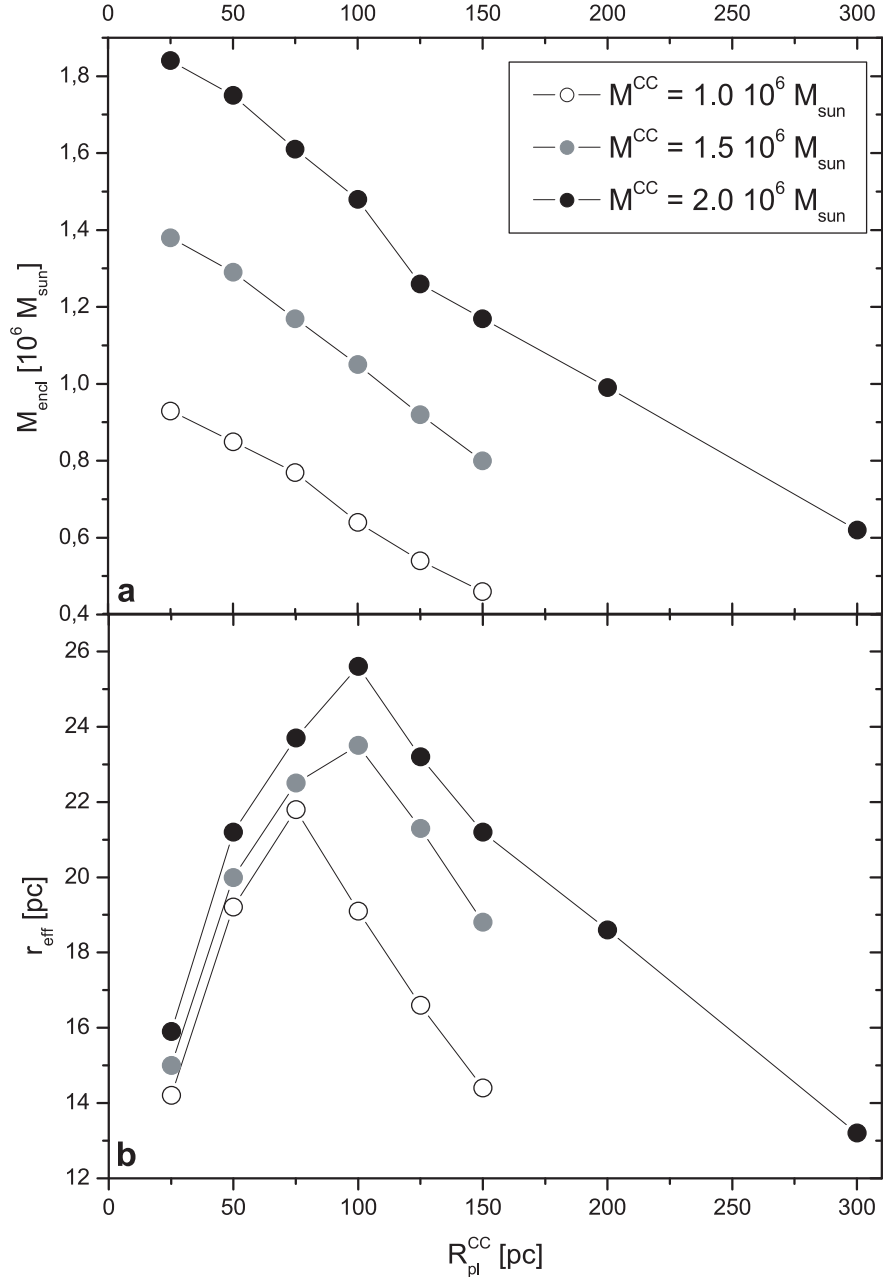


Fig. 7.— **a:** Enclosed mass, M_{endl} , of the merger objects as a function of the initial CC Plummer radius, $R_{\text{pl}}^{\text{CC}}$. **b:** Effective radius, r_{eff} , of the merger objects as a function of the initial CC Plummer radius, $R_{\text{pl}}^{\text{CC}}$.

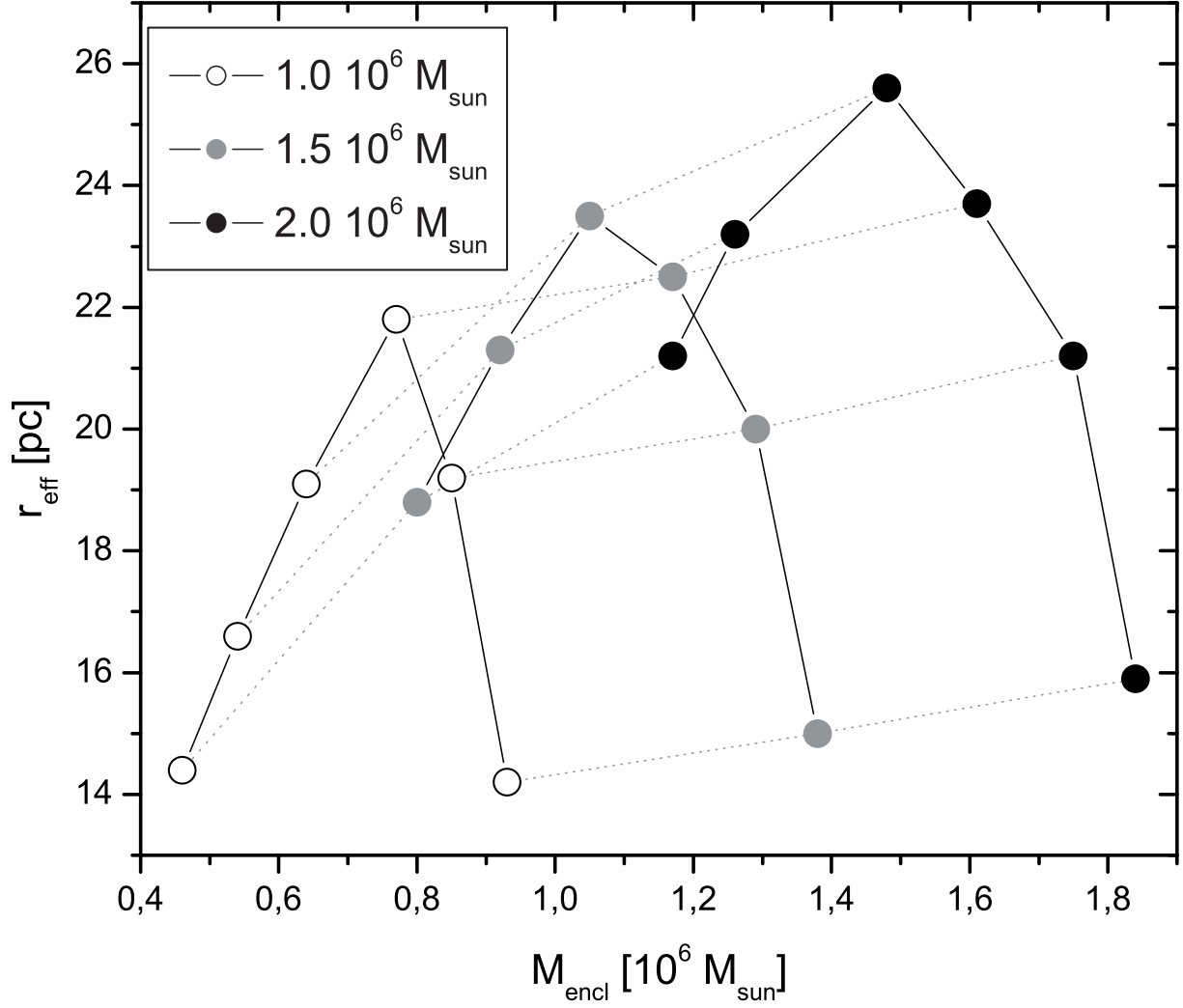


Fig. 8.— Effective radius r_{eff} as a function of the enclosed mass of the merger objects for the CC models with $R_{\text{pl}}^{\text{CC}} = 25, 50, 75, 100, 125,$ and 150 pc (symbols from right to left) and $M^{\text{CC}} = 1.0, 1.5,$ and $2.0 \times 10^6 M_{\odot}$. Models with the same initial CC mass are connected by solid lines. Models with the same $R_{\text{pl}}^{\text{CC}}$ are connected by dotted lines to illustrate the dependence on the initial CC mass.

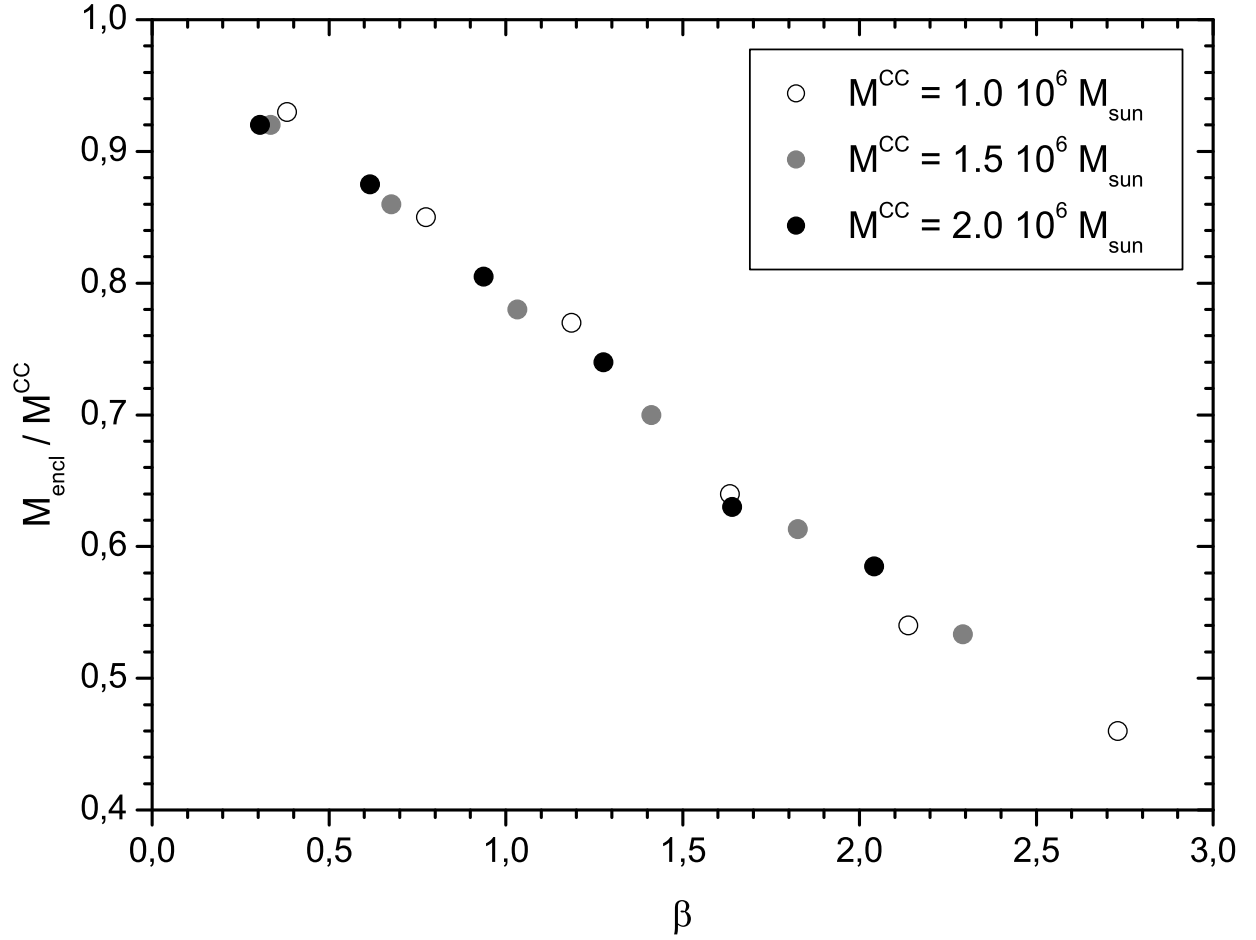


Fig. 9.— The ratio of the merged mass and the initial CC mass, $M_{\text{endl}}/M^{\text{CC}}$, as a function of the parameter β for the models with $R_{\text{pl}}^{\text{CC}} = 25, 50, 75, 100, 125$, and 150 pc.

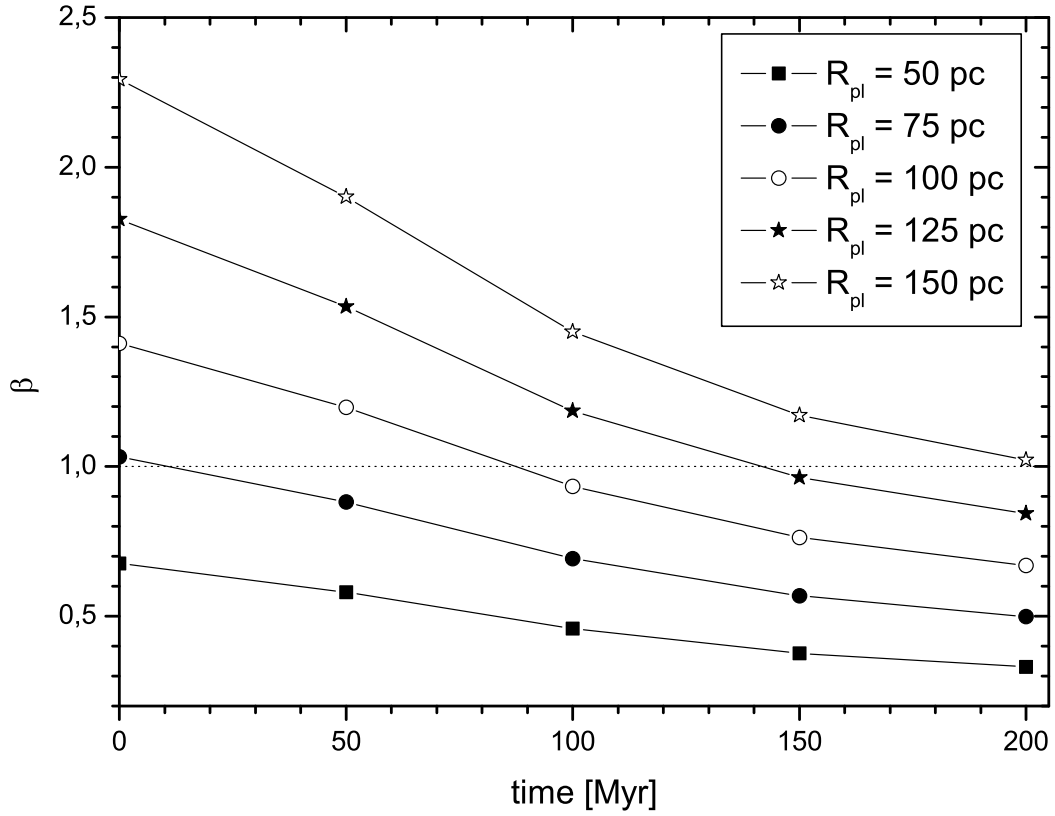


Fig. 10.— Parameter β as a function of time for models with $M^{\text{CC}} = 1.5 \times 10^6 M_{\odot}$ and $R_{\text{pl}}^{\text{CC}} = 50, 75, 100, 125, \text{ and } 150$ pc for the first 200 Myr (the orbital period is about 1.3 Gyr).

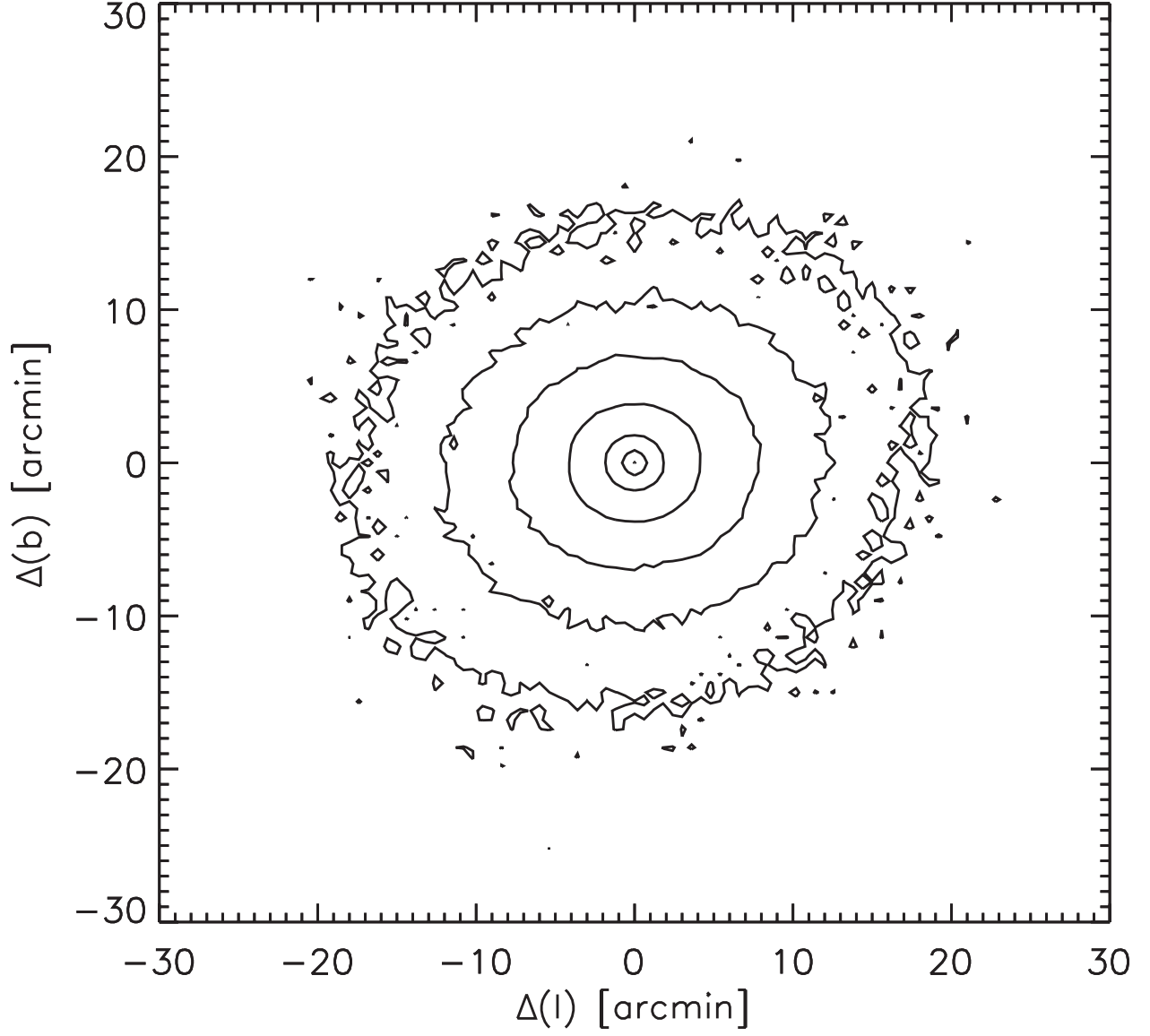


Fig. 11.— Contour plot projected onto the sky in Galactic coordinates for model M_{1-1.5_100} at the current observed position of NGC 2419. The pixel size is 0'.6. The contour levels go from 32 to 20 mag arcsec⁻² in steps of two mag arcsec⁻².

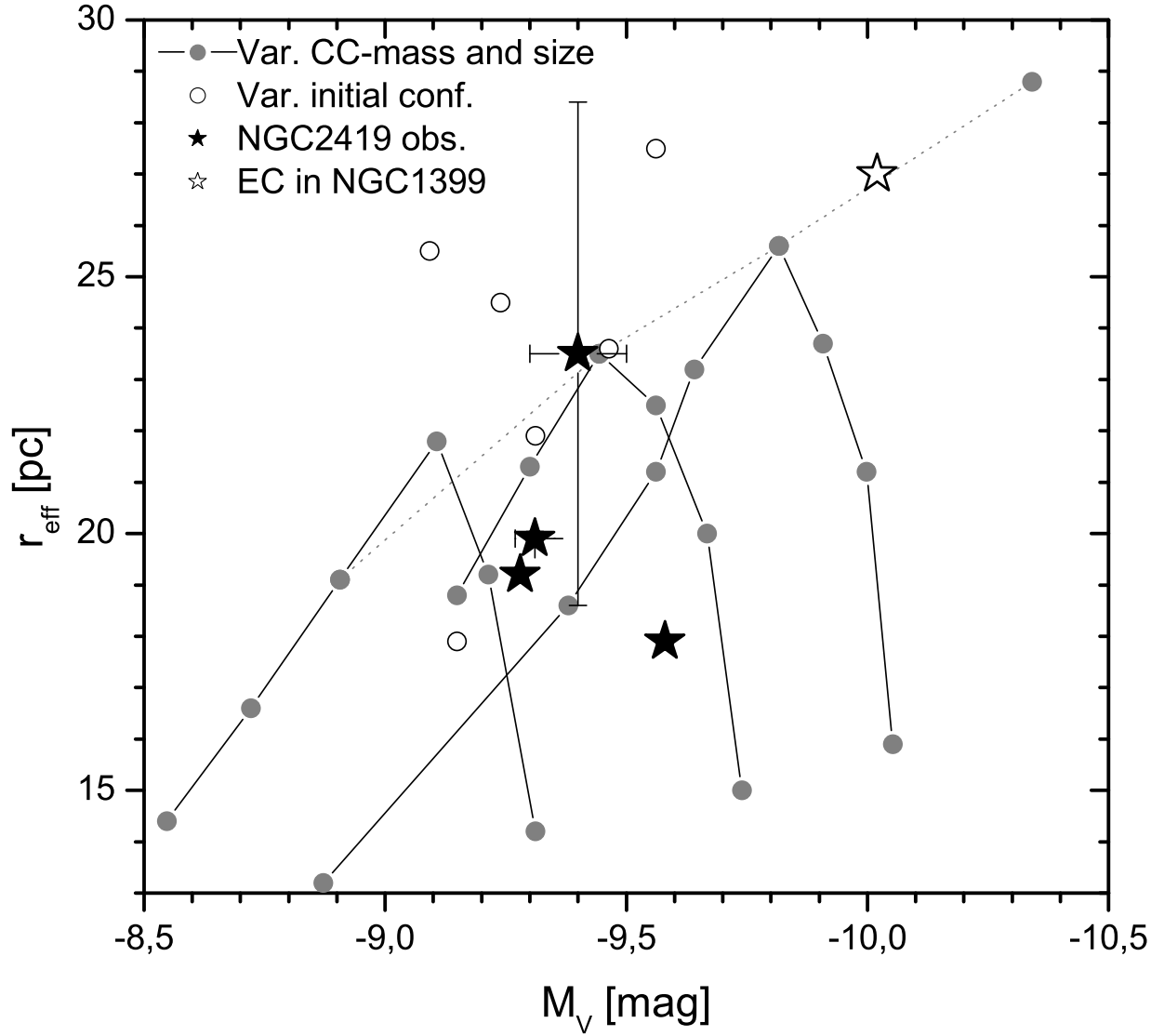


Fig. 12.— Effective radius, r_{eff} , as a function of absolute magnitude, M_V , for all computations (see Table 3, the dotted line connects models with $R_{\text{pl}}^{\text{CC}} = 100$ pc) and observed values of NGC 2419 (black stars). The error bars for the observed values are from the respective papers (see Table 1). In addition, EC 90:12 from NGC 1399 (Richtler et al. 2005) is included (white star).

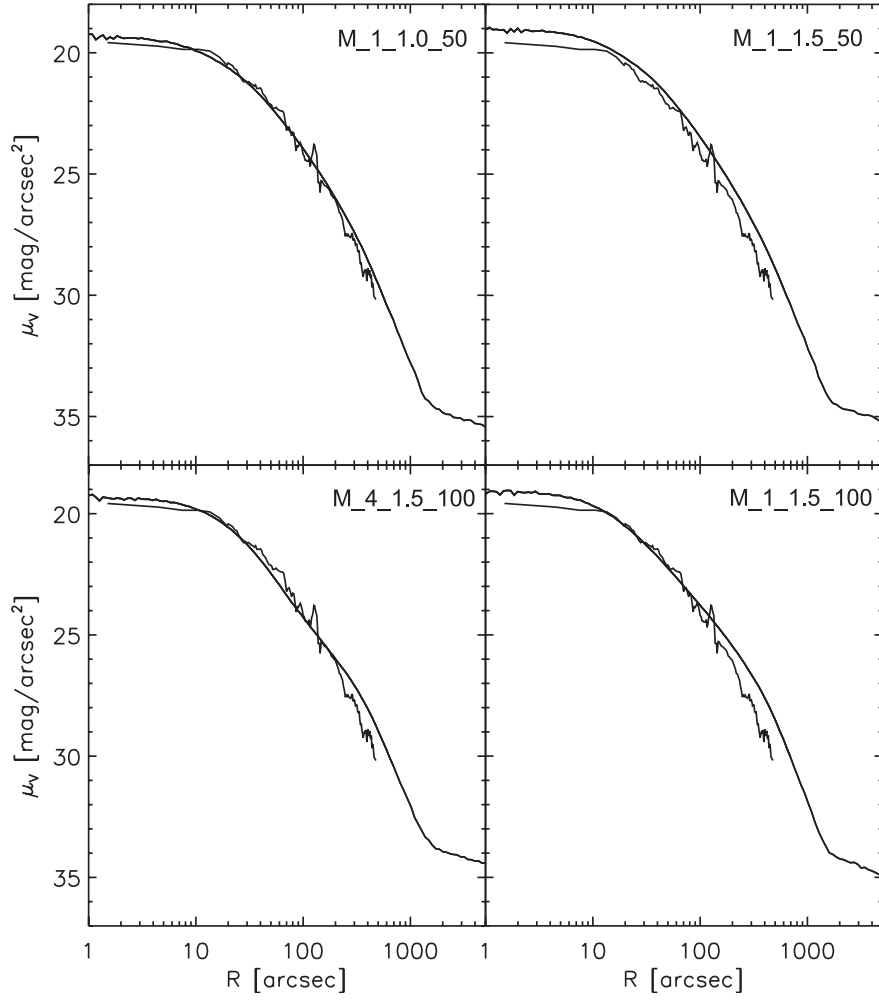


Fig. 13.— Surface brightness profiles of four exemplary models at the current position of NGC 2419 using a mass-to-light ratio of 2.05. A V-band extinction of $A_V = 0.25$ was applied to the models to allow for a direct comparison with the observed surface brightness profile of Bellazzini (2007).

Table 1. Observational Parameters of NGC 2419

	BC ^a	B ^b	MvdM ^c	H ^d
Absolute V magnitude M_V [mag]	-9.28	-9.4	-9.31	-9.58
Total mass ^e [$10^6 M_\odot$]	0.90	1.01	0.93	1.19
Central surface brightness μ_V [mag arcsec ⁻²]	19.61	19.55	19.44	19.83
Core radius r_c [pc]	7.8	7.8	7.9	8.57
Effective radius r_{eff} [pc]	19.2	23.5	19.9	17.88
Tidal radius r_t [pc]	190	174	204	214

^aBaumgardt et al. (2009)

^bBellazzini (2007)

^cMcLaughlin & van der Marel (2005)

^dHarris (1996)

^eusing the mass-to-light ratio of 2.05 from Baumgardt et al. (2009)

Table 2. Initial Cluster Complex and Star Cluster Parameters

	Parameter range
Star Cluster (SC)	
Number of star cluster particles, N_0^{SC}	100 000
Initial SC mass, M^{SC} [$10^5 M_\odot$]	0.5 – 1.5
Plummer radius of the SC, $R_{\text{pl}}^{\text{SC}}$ [pc]	4
Cutoff radius of the SC, $R_{\text{cut}}^{\text{SC}}$ [pc]	20
Cluster Complex (CC)	
Number of star clusters, N_0^{CC}	20
Initial CC mass, M^{CC} [$10^6 M_\odot$]	1.0 – 3.0
Plummer radius of the CC, $R_{\text{pl}}^{\text{CC}}$ [pc]	25 – 300
Cutoff radius of the CC, $R_{\text{cut}}^{\text{CC}}$ [pc]	100 – 1200
α -parameter	0.160 – 0.013

Table 3. Parameters of the Merger Objects

Model ^a	N_M ^b	M_{encl} ^c ($10^6 M_\odot$)	M_V ^d (mag)	r_h ^e (pc)	r_{eff} ^f (pc)	r_c ^g (pc)	μ_V ^h (mag arcsec ⁻²)	σ ⁱ (km s ⁻¹)
M_1_1.0_25	20	0.93	−9.31	18.8	14.2	6.6	18.99	4.88
M_1_1.0_50	20	0.85	−9.21	25.8	19.2	5.7	19.36	4.13
M_1_1.0_75	20	0.77	−9.11	29.8	21.8	5.1	19.41	3.80
M_1_1.0_100	19	0.64	−8.91	24.9	19.1	5.5	19.51	3.59
M_1_1.0_125	16	0.54	−8.72	22.1	16.6	5.0	19.47	3.51
M_1_1.0_150	14	0.46	−8.55	19.6	14.4	4.5	19.39	3.47
M_1_1.5_25	20	1.38	−9.74	19.9	14.9	6.7	18.65	5.85
M_1_1.5_50	20	1.29	−9.67	26.6	20.0	6.2	19.04	4.99
M_1_1.5_75	20	1.17	−9.56	30.1	22.5	5.6	19.12	4.57
M_1_1.5_100	19	1.05	−9.44	31.8	23.5	4.9	19.08	4.34
M_1_1.5_125	17	0.92	−9.30	28.8	21.3	5.3	19.15	4.21
M_1_1.5_150	15	0.80	−9.15	25.1	18.8	4.8	19.09	4.10
M_1_2.0_25	20	1.84	−10.05	21.1	15.9	7.2	18.47	6.55
M_1_2.0_50	20	1.75	−10.00	28.4	21.2	6.4	18.83	5.65
M_1_2.0_75	20	1.61	−9.91	32.0	23.7	6.0	18.88	5.26
M_1_2.0_100	19	1.48	−9.82	35.2	25.6	5.3	18.87	4.99
M_1_2.0_125	16	1.26	−9.64	31.5	23.2	5.4	19.01	4.76
M_1_2.0_150	18	1.17	−9.56	28.9	21.2	5.1	18.81	4.81
M_1_2.0_200	14	0.99	−9.38	26.4	18.6	4.7	18.85	4.64
M_1_2.0_300	10	0.62	−8.87	17.6	13.2	4.8	19.03	4.18
M_1_3.0_100	19	2.40	−10.34	39.6	28.8	5.3	18.45	6.08
M_2_1.5_100	19	1.17	−9.56	37.2	27.5	5.8	19.34	4.24
M_3_1.5_100	19	1.07	−9.46	31.9	23.7	5.3	19.21	4.33
M_4_1.5_100	18	0.80	−9.15	22.7	17.9	5.8	19.23	4.10
M_5_1.5_100	19	0.87	−9.24	31.3	24.5	5.4	19.35	3.84
M_6_1.5_100	15	0.76	−9.09	33.4	25.5	5.2	19.58	3.53
M_7_1.5_200	19	0.93	−9.31	30.1	21.9	5.1	19.12	4.22

^aModel__Configuration__ M^{CC} __ $R_{\text{pl}}^{\text{CC}}$.^bNumber of merged star clusters.

^cEnclosed mass of merger object within 800 pc.

^dAbsolute V-magnitude of merger object.

^eHalf-mass radius of merger object.

^fEffective radius, i.e. the projected half-mass radius of the merger object.

^gCore radius of merger object obtained from a King fit.

^hCentral surface brightness μ_V of merger object obtained from a King fit. An extinction of $A_V = 0.25$ has been applied.

ⁱVelocity dispersion within a projected radius of 100 pc.

Table 4. β -values of our initial CC models

β	25 pc ^a	50 pc	75 pc	100 pc	125 pc	150 pc	200 pc	300 pc
$1.0 \times 10^6 M_{\odot}$ ^b	0.38	0.77	1.19	1.63	2.14	2.73		
$1.5 \times 10^6 M_{\odot}$	0.33	0.68	1.03	1.41	1.83	2.29		
$2.0 \times 10^6 M_{\odot}$	0.31	0.62	0.94	1.28	1.64	2.04	3.02	7.27
$3.0 \times 10^6 M_{\odot}$				1.11				

^aPlummer radius $R_{\text{pl}}^{\text{CC}}$ of the CC.

^bInitial CC mass M^{CC} .